

Feature Learning for Dimensionality Reduction toward Maximal Extraction of Hidden Patterns

Takanori Fujiwara, Yun-Hsin Kuo, Anders Ynnerman, and Kwan-Liu Ma

Abstract— Dimensionality reduction (DR) plays a vital role in the visual analysis of high-dimensional data. One main aim of DR is to reveal hidden patterns that lie on intrinsic low-dimensional manifolds. However, DR often overlooks important patterns when the manifolds are strongly distorted or hidden by certain influential data attributes. This paper presents a feature learning framework, FEALM, designed to generate an optimized set of data projections for nonlinear DR in order to capture important patterns in the hidden manifolds. These projections produce maximally different nearest-neighbor graphs so that resultant DR outcomes are significantly different. To achieve such a capability, we design an optimization algorithm as well as introduce a new graph dissimilarity measure, called neighbor-shape dissimilarity. Additionally, we develop interactive visualizations to assist comparison of obtained DR results and interpretation of each DR result. We demonstrate FEALM’s effectiveness through experiments using synthetic datasets and multiple case studies on real-world datasets.

Index Terms—Dimensionality reduction, feature learning, network comparison, particle swarm optimization, visual analytics.

1 INTRODUCTION

High-dimensional data can contain a rich set of observations measured from phenomena [19]. Dimensionality reduction (DR) constitutes a tool for the understanding of the phenomena by visually revealing patterns in the data and facilitating human interpretation of the patterns [15, 25, 68], leading to important and fundamental insights. Among others, nonlinear DR [80], such as t-SNE [79] and UMAP [59], is especially helpful when the patterns are hidden in nonlinear structures (or manifolds) and infeasible to be found from conventional depictions of data (e.g., with scatterplot matrices, heatmaps, and parallel coordinates [55]).

However, nonlinear DR is sensitive to an attribute’s influence on manifolds. While nonlinear DR is commonly applied to all available attributes, it may fail to capture patterns underlying manifolds that are apparent only in a particular subset of attributes [51]. A similar problem also happens when manifolds are entangled by the relationships among attributes. Although researchers have investigated the effect of attribute selection on linear DR results [72], there is a lack of studies dealing with nonlinear DR as well as the case where manifolds are entangled.

In this work, we complement nonlinear DR methods to enable them to extract various important but subtle patterns in the manifolds embedded in the attributes or combinations of attributes. We first demonstrate that nonlinear DR suffers from the aforementioned problems even when trivial changes in data, such as the inclusion of one additional attribute, are made. We then present a feature learning framework, *FEALM*, designed to discover latent features of data, with which nonlinear DR produces significantly different results from the one using all the available attributes. These latent features can be constructed with a linear projection that is equivalent to a combination of data scaling and transformation, which are commonly used for data preprocessing [28]. *FEALM*’s feature learning is performed through the maximization of the differences between data representations (e.g., nearest neighbor graphs) highly related to nonlinear DR results. Within this framework, we design an exemplifying method for UMAP. We develop an algorithm utilizing particle swarm optimization (PSO) [48] to find latent features to produce maximally different nearest-neighbor graphs, which are intermediate products of UMAP, and consequently generate diverse UMAP results. To detect the difference of the graphs, we introduce a new graph dissimilarity measure, called neighbor-shape dissimilarity (or *NSD*). Using this method, analysts can find multiple relevant UMAP

results that are difficult to find through manual preprocessing of data.

We further develop an interactive visual interface to allow analysts to flexibly seek more patterns and gain insights from them. The interface depicts the similarities of DR results generated during the optimization process to notify unexplored embeddings. Also, through brushing and linking, analysts can conveniently compare multiple DR results. To help review each DR result, our interface integrates an existing contrastive-learning-based interpretation method [25], which highlights characteristics of a group of instances through comparison with others.

We demonstrate the effectiveness of *FEALM*, the exemplifying method, and the visual interface through experiments using synthetic datasets and multiple case studies on real-world datasets. We also conduct a performance evaluation to assess the efficiency of *NSD* and the optimization algorithm. We provide a demonstration video of the interface, detailed evaluation results, and the source code of *FEALM* in the supplementary material at <https://takanori-fujiwara.github.io/s/fealm/>.

In summary, we consider our primary contributions to be:

- a feature learning framework, *FEALM*, designed to extract a set of latent features for nonlinear DR, each of which produces a significantly different DR result;
- an exemplifying method for UMAP, where we introduce a PSO-based algorithm as well as a graph dissimilarity measure, *NSD*;
- a visual interface that assists exploration of DR results and interpretation of each DR result;
- designed examples that illustrate nonlinear DR’s sensitiveness to trivial disturbance to intrinsic manifolds.

2 RELATED WORK

Our work supplements existing DR methods by learning appropriate features from high-dimensional data. Our feature learning optimizes linear transformations through the exploration of various linear subspaces of the original data. We provide the background and relevant works in DR methods and subspace exploration.

2.1 Dimensionality Reduction Methods

DR is widely used for visual exploration of high-dimensional data [23, 64, 68]. Many visualization-purpose DR methods aim to reveal overall data distributions (e.g., variances) or patterns (e.g., clusters) in a low-dimensional space. When only performing a linear projection [17], a DR method is categorized as linear DR. More precisely, it produces an embedding (or representation), \mathbf{Y} , from input data, \mathbf{X} , with $\mathbf{Y} = \mathbf{X}\mathbf{P}$, where $\mathbf{Y} \in \mathbb{R}^{n \times m'}$, $\mathbf{X} \in \mathbb{R}^{n \times m}$, $\mathbf{P} \in \mathbb{R}^{m \times m'}$, and n, m, m' are the numbers of instances, attributes, and latent features, respectively (usually $m' \ll m$). For example, principal component analysis (PCA) [36, 45] and classical multidimensional scaling (MDS) [75] are well-known linear DR methods. While linear DR only captures the linear structure of \mathbf{X} , nonlinear

• Takanori Fujiwara and Anders Ynnerman are with Linköping University.
E-mail: {takanori.fujiwara, anders.ynnerman}@liu.se.
• Yun-Hsin Kuo and Kwan-Liu Ma are with University of California, Davis.
E-mail: {yskuo, klma}@ucdavis.edu.

DR uncovers the nonlinear structure [80]. For example, t-SNE [79] and UMAP [59] aim to preserve local neighborhoods of each instance, which is often a difficult task when relying only on a linear projection.

Despite the frequent use of the aforementioned DR methods for visual analytics [68], they may fail to show important patterns when data contains noises or influential attributes to the overall data distribution. Several DR methods have been developed to address this limitation. For example, discriminant analysis [34, 41, 61], such as linear discriminant analysis (LDA), utilizes class information to reduce noises that are irrelevant to class separation. Contrastive learning [89], such as contrastive PCA [2], compares two datasets to reveal patterns that are more salient in one dataset compared to another. Unified linear comparative analysis [27] flexibly incorporates the strengths of both discriminant analysis and contrastive learning. However, all these methods require additional information (e.g., class labels) and focus only on revealing patterns related to a specific interest (e.g., classification). Thus, these methods would not be suitable when performing an early-stage exploration without complete knowledge of data and/or expected findings, which is an important task that visual analytics should support.

Other than visualization, some of DR methods can be utilized for feature selection and feature learning [87]. For example, PCA and LDA are frequently used in data preprocessing for subsequent machine learning (ML) methods, such as deep neural networks or even other DR methods (e.g., t-SNE and UMAP), as reducing dimensions is helpful to avoid high computational costs and the curse of dimensionality. As shown in comprehensive survey by Zebari et al. [87], a large portion of this type of DR targets on classification tasks.

FEALM can be seen as an unsupervised linear DR method for feature learning. We design FEALM to preprocess data to produce significantly different nonlinear DR results from one obtained using original data as is. FEALM does not require additional information, such as class labels; thus, it supports an early-stage exploration.

2.2 Exploration of Axis-Parallel Subspaces

There are two major types of subspaces: axis-parallel subspaces and linear subspaces. Axis-parallel subspaces are composed of a subset of original data attributes. Thus, there are 2^m subspaces we can explore (m : the number of attributes). On the other hand, linear subspaces consist of axes obtained through linear projections of original data. Although linear subspaces embrace axis-parallel subspaces, here we only describe studies on axis-parallel subspaces and the rest in Sect. 2.3.

Scatterplot matrices [33] and parallel coordinates [40] are classic visualizations to explore axis-parallel subspaces. A set of methods have been developed to improve these visualizations' scalability and usability [18, 50, 84, 86]. In response to the increase in the available number of data attributes, more efforts have been devoted to comparing a large set of subspaces. A common approach is finding meaningful subspaces with subspace selection [8], visualizing each subspace's dissimilarity, and informing patterns seen in each subspace with DR [39, 42, 62, 74, 82]. While this approach uses DR to understand subspaces, Sun et al. [72] investigated subspace selection's influences on PCA and MDS results. More comprehensive descriptions of relevant works can be found in a survey by Liu et al. [55].

Subspace clustering [51, 65] in the ML field shares a closely related concept with our work. Subspace clustering aims to find clusters within axis-parallel subspaces. By limiting the use of data to a subset of attributes, subspace clustering can uncover clusters that are hidden by irrelevant attributes. Note that, in the visualization field, "subspace clustering" is often confusingly used to represent clustering of subspaces; however, in standard ML terminology, subspace clustering performs clustering *within* axis-parallel subspaces.

Our work seeks subspaces that produce significantly different nonlinear DR results to reveal hidden patterns. The work by Sun et al. [72] and subspace clustering methods [51, 65] are closely related to our work in terms of analyzing the subspace change's influence on data patterns. However, our work is for the use with nonlinear DR methods and provides optimization and visualization methods to find appropriate linear subspaces, which do not limit to axis-parallel subspaces.

2.3 Exploration of Linear Subspaces

To show high-dimensional data distributions in a selected 2D linear subspace (or 2D view [29]), scatterplots and star coordinates are often used, with interactive enhancements [5, 55, 83]. We can see linear DR as a method that selects a view suitable to see some characteristics of data (e.g., variance with PCA). For this usage, linear DR is sometimes called projection pursuit [38, 47]. Various interactive adjustment methods for linear DR have been introduced, as summarized in multiple surveys [64, 68]. For example, iPCA [44] allows interactive updates of each attribute's contribution to a PCA result.

When dealing with many attributes, manually finding informative subspaces becomes almost infeasible. Thus, researchers have designed (semi)automatic and visual recommendations. For example, Wang et al. [83] utilized LDA to suggest star coordinates that show clear cluster separations. Zhou et al. [88] visualized the similarities of original attributes as well as 1D subspaces to help analysts construct interesting subspaces. Liu et al. [56] visualized the similarities of multidimensional subspaces, using the Grassmann distance. Gleicher et al. [29] utilized support-vector machines to suggest simple linear subspaces that satisfy specifications provided by analysts. Grassmannian Atlas [54] provides an overview of projection qualities (e.g., skewedness) of all 2D subspaces sampled from the Grassmannian manifold. Lehmann and Theisel [53] developed an optimization method to provide a set of 2D subspaces that are significantly different from each other.

Lehmann and Theisel's work [53] is the most related work as they also aimed to mine various patterns in different subspaces. While theirs only finds and visualizes 2D subspaces (i.e., equivalent to linear DR onto 2D planes), ours searches multidimensional subspaces and uses them as nonlinear DR inputs to uncover patterns hidden in complex data.

3 MOTIVATING EXAMPLES

Using UMAP [59] as a representative nonlinear DR method, we provide concrete cases where nonlinear DR misses important data patterns. The datasets that we created, source code for the data generation, and comprehensive experiment results are made available in the supplementary materials [1]. As shown in Fig. 1-a, we first generated a dataset with three attributes, with which instances are placed around two different spherical surfaces. This dataset has approximately 200 blue (Sphere 1) and 100 orange (Sphere 2) instances. The inner sphere corresponding to Sphere 2 has a radius with 40% length of the outer sphere's radius. Also, small noises are added for the placement of each instance.

When visualizing this dataset in a 2D space, linear DR can only produce a plane cut of the 3D spheres; consequently, we cannot see a clear distinction between them (Fig. 1-b). Any linear DR causes a similar issue when data has curved shapes, such as those in the well-known Swiss-Rolls dataset [57]. On the other hand, nonlinear DR methods that aim to preserve each instance's local neighbors such as t-SNE and UMAP can separate Spheres 1 and 2, as shown in Fig. 1-c.

However, even nonlinear DR easily fails to find important patterns when some attributes affect manifolds that contain the corresponding patterns. This situation can happen even with subtle changes in a dataset. To illustrate this, as shown in Fig. 1-d, we generated a new dataset by adding one attribute that has three classes (Classes A-C) having clearly different values. We shuffled the order of the 3-class attribute's instances (i.e., there are no correspondence among Spheres 1-2 and Classes A-C). Also, we applied the Z-score normalization for each attribute to follow the standard preprocessing for DR [46] and to avoid creating strong influences from the 3-class attribute. UMAP results for this dataset are presented in Fig. 1-e, f. We can see that UMAP does not show the separation of Spheres 1 and 2 anymore. Moreover, UMAP does not clearly distinguish Classes A-C either. Similar issues happen even when using other nonlinear DR methods, such as t-SNE. Also, hyperparameter adjustments of UMAP, such as k used for the k -nearest neighbor (k -NN) graph construction, cannot solve this issue as the manifold itself is distorted (for details, refer to [1]).

The issue seen in this dataset (Fig. 1-d) can be solved by assigning larger weights to the 2-sphere attributes (or excluding the 3-class attribute), which leads to a clear separation of Spheres 1-2. Similarly, by assigning a large weight only to the 3-class attribute, DR can find

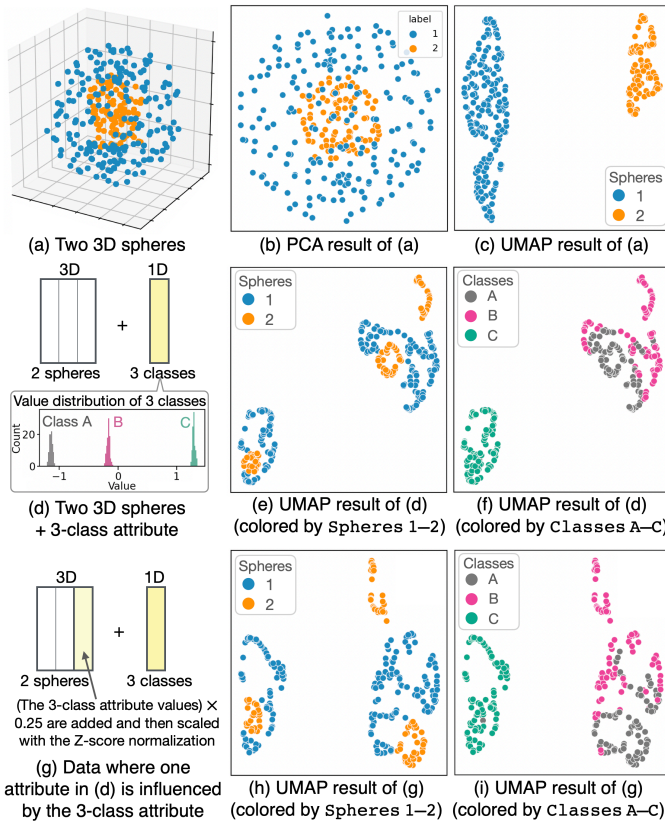


Fig. 1: Three datasets (a,d,g) and PCA (b) and UMAP results (c,e,f,h,i).

Classes A–C. In fact, our method for UMAP, which we introduce in Sect. 5, can reveal these two patterns by automatically adjusting the weights. Fig. 2 shows four examples suggested by our method. The results are produced with the same UMAP’s hyperparameters as the ones used in Fig. 1. In Fig. 2-d1, by using a relatively small weight for the 3-class attribute (i.e., 0.4), UMAP shows clear clusters of Spheres 1–2. Similarly, Fig. 2-c2 shows three clusters of Classes A–C by assigning the 3-class attribute a large weight (i.e., 1.9).

The above issue can be more complicated when patterns are entangled in multiple attributes’ relationships. We create a dataset exhibiting such features by adding 25% portions of the 3-class attribute values into one of the 2-sphere attributes and then applying the Z-score normalization again, as described in Fig. 1-g. This type of entanglements can be found in, for example, income statistics partially influenced by age and a political opinion influenced by a voter’s general ideology. The attribute weighting or selection cannot resolve the features in this dataset. Fig. 3-a1, a2 show UMAP results on this dataset after removing the 3-class attribute, which still do not show the separation of Spheres 1 and 2. However, this can be solved by learning latent features by our method. The right three columns of Fig. 3 show a subset of the generated UMAP results. We can see d1 and b2 clearly separate Spheres 1–2 and Classes A–C, respectively.

The above examples demonstrate that nonlinear DR can easily overlook important, obvious data patterns when certain attributes influence intrinsic manifolds—even a single attribute can cause this situation. While the examples are the case for finding distinct data groups, similar issues can happen even when an analysis aim is to find, for example, continuous value changes on manifolds as in the Swiss-Rolls dataset.

4 FEALM FRAMEWORK

This section introduces a feature learning framework, *FEALM*, to address the aforementioned issues in nonlinear DR. We name the framework *FEALM* because it performs *FEATure Learning* to capture or *film* patterns underlying hidden Manifolds. As the problem can be extremely complicated based on the combinations of DR methods, their hyperparameters, and hidden manifolds we should consider, we first

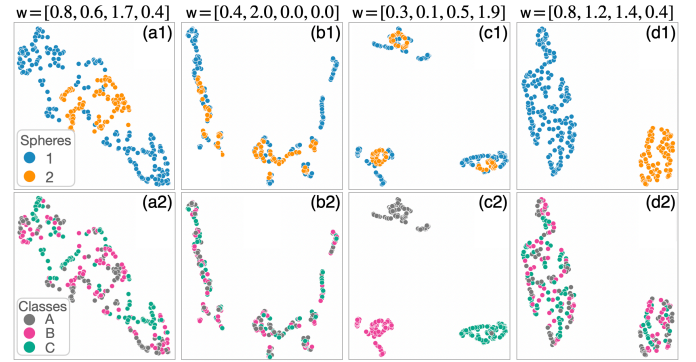


Fig. 2: UMAP results of the dataset shown in Fig. 1-d after using our feature learning method. w shows the attribute weights.

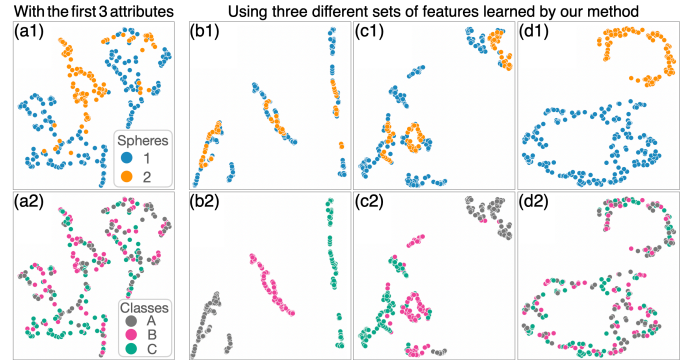


Fig. 3: UMAP results of the dataset shown in Fig. 1-g after selecting only the first three attributes (a) and using our feature learning method (b–d).

specify our scope. We then describe the architecture of *FEALM*, where a projection matrix is optimized with the following steps: (1) transforming data with the current projection matrix, (2) generating graph or low-dimensional representations of the transformed data, (3) evaluating the projection matrix based on the dissimilarity of the representations, and (4) updating the projection matrix based on the evaluation.

4.1 Problem Scope

FEALM aims to supplement *nonlinear DR* methods, even more specifically, for those construct a *graph-based* data representation as the intermediate product or generate DR results highly related to such a representation. This scope is reasonable and still provides enough flexibility in *FEALM* because many DR methods can be considered graph-based [59, 79, 85]. Such methods include metric/non-metric MDS [69], the Barnes-Hut t-SNE (common t-SNE implementation) [78], and UMAP [59]. For example, metric and non-metric MDS constructs a dissimilarity matrix of instances, which can be converted to a kernel/similarity matrix—corresponding to a weighted graph where nodes and edges represent instances and their similarities, respectively. The Barnes-Hut t-SNE and UMAP perform DR based on a similarity/weighted graph derived from the k -NN graph of instances.

FEALM searches significantly different DR results for a *given DR method* with *given hyperparameters*. *FEALM* is not designed to select a DR method nor hyperparameters to reveal hidden patterns.

FEALM can only find patterns underlying (nonlinear) manifolds that exist in a *linear subspace* of the original data. We set this scope because of two reasons. First, we do not want to allow unintuitive or excessive data manipulation not only to provide more interpretable data preprocessing but also to avoid leading to false patterns as much as possible. A linear projection only allows a set of linear transformations that can be converted into a single matrix multiplication (i.e., $Y = XP$, as described in Sect. 2.1). Based on analysts’ demands, *FEALM*’s linear projection can be limited to data scaling (or attribute weighting), orthogonal transformation (similar to PCA), and a combination of both, all of which are commonly used for data preprocessing. Second, finding hidden manifolds that do not exist in a linear projection of data is computationally challenging. Such manifolds might be able to

find, for example, by utilizing neural networks; however, this approach requires expensive parameter tuning.

4.2 Optimization Architecture

We describe the architecture of FEALM designed with considerations of flexibility and computational efficiency.

Forms of the problem. For input data, $\mathbf{X} \in \mathbb{R}^{n \times m}$ (n, m : the numbers of instances and attributes), latent features can be computed with \mathbf{XP}_i , where $\mathbf{P}_i \in \mathbb{R}^{m \times m'}$ (m' is the number of latent features and $m' \leq m$) is a projection matrix. With f_{DR} , a function that performs DR with a given method and hyperparameters, we can obtain a DR result or embedding, \mathbf{Y}_i , i.e., $\mathbf{Y}_i = f_{\text{DR}}(\mathbf{XP}_i)$. We can measure a dissimilarity of two DR results, \mathbf{Y}_i and \mathbf{Y}_j , with a certain function, $d_{\text{DR}}(\mathbf{Y}_i, \mathbf{Y}_j)$ (e.g., the Frobenius norm). Let \mathbf{Y}_0 be a DR result using \mathbf{X} as is (i.e., $\mathbf{Y}_0 = f_{\text{DR}}(\mathbf{X})$). Then, we can write an optimization problem to find \mathbf{P}_1 that generates \mathbf{Y}_1 maximally different from \mathbf{Y}_0 as: $\arg\max_{\mathbf{P}_1} d_{\text{DR}}(\mathbf{Y}_1, \mathbf{Y}_0)$. When iteratively finding a new projection matrix, \mathbf{P}_{i+1} , we want to find one that generates \mathbf{Y}_{i+1} maximally different from a set of DR results already produced, $\mathcal{Y}_i = \{\mathbf{Y}_0, \dots, \mathbf{Y}_i\}$. With some reduce function, Φ (e.g., mean), the problem of finding \mathbf{P}_{i+1} can be written as:

$$\arg\max_{\mathbf{P}_{i+1}} \Phi(d_{\text{DR}}(\mathbf{Y}_{i+1}, \mathbf{Y}_0), \dots, d_{\text{DR}}(\mathbf{Y}_{i+1}, \mathbf{Y}_i)). \quad (1)$$

Note that Eq. 1 shares some similarities with the one presented by Lehmann and Theisel [53]. However, their optimization is only to produce 2D linear DR results, and their case limits to $\mathbf{Y}_i = \mathbf{XP}_i$ ($\mathbf{P}_i \in \mathbb{R}^{m \times 2}$). Also, they only use the extended version of the Procrustes distance [30] and Frobenius norm as a combination of d_{DR} and Φ (for more details, refer to [53]). FEALM can be used for nonlinear DR and provides flexibility for each function choice. For Φ , rather than computing a norm or maximum, we recommend taking a minimum of dissimilarities (i.e., Eq. 1 maximizes the minimum of dissimilarities). With this, we can find a DR result that is different from all the existing results and avoid a case where the optimization keeps producing the same or similar results (e.g., a case where \mathbf{Y}_0 has an extremely larger dissimilarity with \mathbf{Y}_1 than with other potential DR results). We provide a graphical explanation of such cases in the supplementary materials [1].

While Eq. 1 is a straightforward description of our goal, directly performing this optimization for nonlinear DR methods is often difficult because for two-folded reasons. First, f_{DR} is often computationally expensive. For example, UMAP took 5 seconds to produce Fig. 1-h from the data containing only 300 instances and 4 attributes. If the optimization requires many trials, completion time can easily surpass several hours (e.g., about 1.5 hours for 1,000 trials). Second, popularly used nonlinear DR methods such as t-SNE and UMAP contain randomness in f_{DR} . For example, random initialization of an embedding (as in t-SNE) or random sampling during the optimization (as in UMAP) highly influences the final result [49]. Consequently, it becomes difficult to adjust \mathbf{P}_i during the optimization—when the objective value of Eq. 1 becomes better, we do not know whether it is the improvement from changes in \mathbf{P}_i or caused by the randomness in f_{DR} .

Thus, FEALM also introduces an optimization problem that maximizes the differences among graph representations of data. Here we can use graph representations that are the same with or similar to intermediate products of a given nonlinear DR. This optimization is based on a general observation: if such graph representations have maximal differences, derived DR results are also significantly different. Let f_{Gr} be a function that generates some graph (e.g., k -NN graph, similarity matrix) from an input matrix. Then, a graph, G_i , corresponding to \mathbf{P}_i can be obtained with $G_i = f_{\text{Gr}}(\mathbf{XP}_i)$. Also, we denote a function that measures a dissimilarity of two graphs, G_i and G_j , as $d_{\text{Gr}}(G_i, G_j)$. With a set of already produced graphs, $\mathcal{G}_i = \{G_0, \dots, G_i\}$, we can write a relaxed version of the optimization problem:

$$\arg\max_{\mathbf{P}_{i+1}} \Phi(d_{\text{Gr}}(G_{i+1}, G_0), \dots, d_{\text{Gr}}(G_{i+1}, G_i)). \quad (2)$$

When developing a method within FEALM, we can choose Eq. 1 or 2 based on the characteristics of a DR method, such as the computational efficiency and stability. We can also use Eq. 1 and 2 in a hybrid manner.

For example, we can generate a large amount of projection matrices with Eq. 2 and then filter them with Eq. 1 to obtain refined results.

Constraints on a linear projection. Another important consideration of the optimization is the constraints on \mathbf{P}_i . We should decide the constraints based on data manipulation allowed for an analysis goal and the optimization difficulty for a given dataset (Sect. 6 provides the detailed discussions). Here we list representative options: (1) no constraint; (2) allowing only data scaling; (3) allowing data scaling and orthogonal transformation. With any option, we can interpret how linear transformed data is generated by reviewing values in \mathbf{P}_i .

When there is (1) no constraint in a projection matrix, \mathbf{P} , FEALM most flexibly learns features. However, as there is no guarantee that the learned features have orthogonality with each other, distance-related functions (e.g., k -NN graph construction using the Euclidean distance) might not work in an intended way. Also, the optimization needs to search the best values for $m \times m'$ parameters in \mathbf{P} .

When (2) allowing only data scaling, $\mathbf{P} = \text{diag}(\mathbf{w})$ where \mathbf{w} is an m -length vector. Practically, we can restrict $\mathbf{w} = \sqrt{m}\mathbf{u}$ where \mathbf{u} is a unit vector. When \mathbf{u} consists of uniform values, $\mathbf{w} = [1, \dots, 1]$ (i.e., performing no scaling). Then, \mathbf{w} can be identified by searching a unit vector. This constraint is used when generating the results in Fig. 2. As this search is only on m parameters, finding the best \mathbf{P} is much easier than the case with no constraint.

With (3) the last constraint, $\mathbf{P} = \text{diag}(\mathbf{w})\mathbf{M}\text{diag}(\mathbf{v})$, where $\mathbf{M} \in \mathbb{R}^{m \times m'}$ is an orthogonal matrix (i.e., $\mathbf{M}^T\mathbf{M} = \mathbf{I}_{m'}$; $\mathbf{I}_{m'}$ is an $m' \times m'$ identity matrix) and \mathbf{v} is an m' -length vector. Here \mathbf{M} ensures that $\mathbf{M}\text{diag}(\mathbf{v})$ generates orthogonal features of $\mathbf{X}\text{diag}(\mathbf{w})$. And, \mathbf{v} weights the features to control their influence on a projection. Similar to \mathbf{w} , we can decompose \mathbf{v} with $\mathbf{v} = \sqrt{m'}\mathbf{u}'$, where \mathbf{u}' is a unit vector. A projection under this constraint resembles a combination of standard data preprocessing steps (i.e., data scaling and orthogonal data transformation). This constraint still needs to find best $m \times m'$ parameters.

General optimization strategies. Eq. 1 and 2 can be considered as the optimization over manifolds (or often called manifold optimization) [3, 17, 76]. For example, for the aforementioned constraint (1), \mathbf{P} can be found from the Euclidean manifold. A solution under the constraint (2) is derived by finding \mathbf{u} from a unit sphere manifold [4]. Lastly, for the constraint (3), we can find \mathbf{u}, \mathbf{u}' from unit sphere manifolds and \mathbf{M} from the Grassmann manifold [3] that is a manifold of m' -dimensional subspaces of m -dimensional space. To perform manifold optimization, we can utilize existing libraries, such as Pymanopt [76]. These libraries can help us, for example, generate parameters on a specified manifold.

To solve the optimization, when all functions involved in Eq. 1 (or Eq. 2) are differentiable, we can utilize automatic differentiation together with a solver for differentiable functions (e.g., gradient descent) through existing libraries, such as JAX [13] and Pymanopt [76]. When some functions are not differentiable (e.g., k -NN graph construction), we can use a derivative-free solver, such as PSO.

In addition to the optimization problem, constraints, and solver, we need to select or design f_{Gr} , d_{Gr} , and/or d_{DR} based on a DR method.

5 EXEMPLIFYING METHOD

We design an exemplifying method for UMAP, using FEALM. In the rest of the paper, we denote this method *FEALM-UMAP*. We chose UMAP because it is computationally rather efficient (e.g., when compared with t-SNE) [59] and frequently used for visualization in various applications [9, 20, 35]. The specific designs for UMAP can also be generalized and easily adapted to other DR methods. For example, we expect that a method for t-SNE can be developed based on FEALM-UMAP with minor adjustments in f_{Gr} .

5.1 Graph Generation Function

UMAP processes data in two steps: graph construction and graph layout. Through iterative optimization, the graph layout process performs the placement of instances (usually in 2D) based on a constructed graph. This iterative optimization involves random sampling and expensive computations. Thus, we design a method using Eq. 2, which requires f_{Gr} and d_{Gr} . During the graph construction process, UMAP computes the instance dissimilarities (by default, using the Euclidean distance)

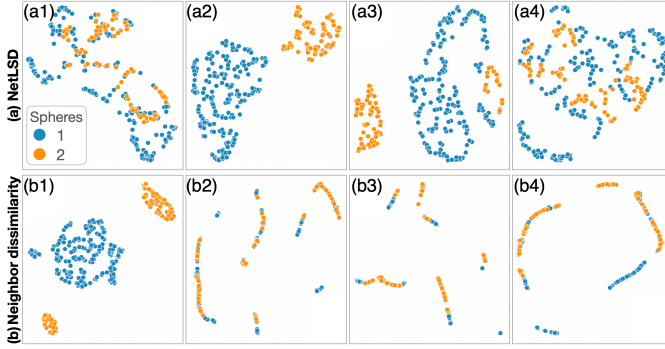


Fig. 4: UMAP results of the dataset shown in Fig. 1-d, using the same settings with Fig. 2 except for d_{Gr} . While Fig. 2 is generated with NSD, here we use NetLSD (a) and the neighbor dissimilarity (b).

and then produces a k -NN graph based on the dissimilarities. Afterward, UMAP constructs a fuzzy graph, which is a weighted graph where the dissimilarities are converted to the fuzzy topological representation (refer to [59] for details). From this fact, f_{Gr} can be the generation of a k -NN or fuzzy graph. While a fuzzy graph contains richer information of instances' relationships, many of the state-of-the-art graph dissimilarity measures, including those we utilize to design our measure, are only available for unweighted graphs [52, 58, 73]. Therefore, we use f_{Gr} that generates a **k -NN graph**; however, we can replace this with a fuzzy graph once d_{Gr} suitable for weighted graphs is developed.

5.2 Graph Dissimilarity Measure

We can select a dissimilarity measure for unweighted graphs based on analysis interest. When using nonlinear DR for visualization, however, we usually want to reveal patterns that are visually apparent and related to the instances' neighborhood relationships (i.e., *shape* and *neighbors*), such as clusters and outliers [14, 64]. Another critical consideration is computational efficiency as graph comparison itself is often expensive. But, it is often difficult to judge only based on theoretical time complexity because of their detailed implementation differences (e.g., requiring only fast matrix operations or slow iterative loops). Based on our experiments [1], we identify that NetLSD [77] can better capture differences of graph shapes with a greatly shorter runtime than many other measures available in a library of graph dissimilarities [58] (despite NetLSD's high time complexity, $\mathcal{O}(n^3)$). NetLSD does not consider the neighbor dissimilarity; thus, for d_{Gr} , we introduce a new measure, **NSD**, to capture both neighbor and shape dissimilarities.

5.2.1 Neighbor-Shape Dissimilarity (NSD)

We design a neighbor dissimilarity measure, **ND**, and combine it with NetLSD to introduce **NSD**. Fig. 2 and Fig. 4 demonstrate how these measures affect DR results when applying FEALM-UMAP to the same dataset. For example, as seen in Fig. 4-b, ND only considers the changes of k -neighbors around each instance; as a result, they tend to form string shapes, where the orders of adjacent nodes are likely different. On the other hand, the results with NetLSD (Fig. 4-a) show four unique shapes; however, for example, a1 and a4 do not likely have many neighborhood changes. Although we need more investigations to precisely conclude these tendencies, due to their algorithms, NetLSD and ND can only address the shape and neighbor differences, respectively. When using NSD (Fig. 2), we can find patterns related to both types of changes.

For the neighbor dissimilarity, one option is to utilize the steadiness and cohesiveness (SnC) [43], which are developed to assess the DR quality by measuring the changes of the neighborhood relationships in the original data and a DR result. While SnC is adaptable to graph comparison, it involves random-walk-based sampling and expensive clustering steps. Thus, similar to the reasons why using Eq. 2 instead of Eq. 1, SnC is not suitable for use in the optimization. Inspired by SnC, we design ND based on shared-nearest neighbor (SNN) similarity [22].

SNN similarity measures how much of neighbors are shared in each pair of instances in a graph. Let \mathbf{A} be a directed adjacency matrix containing the information of each instance's k -NNs. Then, all instance

pairs' SNN similarities, \mathbf{S} , can be computed with $\mathbf{S} = \mathbf{A}\mathbf{A}^\top/k$. Given two graphs, G_i and G_j , we can obtain the difference of each instance's SNN similarity with $\mathbf{D}_{i,j} = \mathbf{S}_i - \mathbf{S}_j$. Let $\mathbf{D}_{i,j}^+$ and $\mathbf{D}_{i,j}^-$ be matrices only taking positive and negative values of $\mathbf{D}_{i,j}$, respectively. Then, $\mathbf{D}_{i,j}^+$ and $\mathbf{D}_{i,j}^-$ capture the increase and decrease of SNNs for each instance in G_i when compared to G_j , respectively. We can compute the total increase and decrease with the Frobenius norm, i.e., $\|\mathbf{D}_{i,j}^+\|_F$ and $\|\mathbf{D}_{i,j}^-\|_F$. Lastly, to reduce them into one value, we take the maximum of them. That is, ND of G_i and G_j is defined as:

$$d_{ND}(G_i, G_j) = \max(\|\mathbf{D}_{i,j}^+\|_F, \|\mathbf{D}_{i,j}^-\|_F). \quad (3)$$

Unlike SnC, ND involves only simple matrix computations while keeping a similar strength to SnC to capture the neighbor dissimilarity. We compare SnC and ND in Sect. 6.

Let d_{SD} ($d_{SD} \geq 0$) be the shape dissimilarity measure using NetLSD. Since NetLSD is only for undirected, unweighted graphs, we use undirected k -NN graphs as NetLSD's inputs (i.e., instead of \mathbf{A} , $\mathbf{A} + \mathbf{A}^\top - \mathbf{A} \circ \mathbf{A}^\top$, where \circ is the Hadamard product). Then, we define the dissimilarity measured by NSD as:

$$d_{NSD}(G_i, G_j) = d_{ND}(G_i, G_j)^\beta \cdot \log(1 + d_{SD}(G_i, G_j)) \quad (4)$$

where $d_{NSD}(G_i, G_j) \geq 0$ and β ($0 \leq \beta \leq \infty$) is a hyperparameter that controls how strongly NSD focuses on the neighbor dissimilarity v.s. the shape dissimilarity. When $\beta = 0$, NSD is equivalent to using NetLSD. As β increases, ND becomes more influential on NSD. Based on our experiment, we set $\beta = 1$ by default. β can be adjusted based on what kind of patterns we look for. Also, since NetLSD involves an exponential function when computing the dissimilarity (refer to [77]), we take a logarithm of $1 + d_{SD}$ (1 is added to avoid taking a logarithm of 0) to avoid excessive influence from the shape difference.

5.3 Optimization

FEALM-UMAP optimizes Eq. 2 while using the k -NN graph construction as f_{Gr} and d_{NSD} as d_{Gr} . As recommended, we use Φ to take a minimum of the dissimilarities. For the constraints of a linear projection, FEALM-UMAP supports all the three representative options described in Sect. 4.2. Since the k -NN graph construction is a non-differentiable function, we develop a **PSO-based derivative-free solver**. We provide pseudocode in the supplementary material [1].

Unlike gradient descent and other optimization algorithms, PSO [48] uses a group of agents, called a swarm of particles, to find the best solution. Particles are initialized with various solutions (e.g., with random initialization) and each of them iteratively moves forward to a direction along which a better solution can be likely found. Also, at each iteration, particles communicate with each other to guide them to better solutions. After the final iteration, PSO returns the best solution so far. For our problem, particles need to travel on multidimensional manifolds. Thus, to cover wide space as much as possible while maintaining a reasonable completion time, we recommend producing a large number of particles but using a small number of iterations (e.g., 500 particles and 20 iterations). Random initialization of particles and restriction of their movement on a specified manifold (e.g., the Grassmann manifold) can be easily achieved by utilizing the manifold optimization libraries [12, 76]. By repeating the above optimization r times, we can obtain a set of projection matrices, $\mathcal{P} = \{\mathbf{P}_0, \dots, \mathbf{P}_r\}$.

Utilization of non-best solutions. To find various patterns, ideally, we should produce a large \mathcal{P} . However, the completion time of the optimization linearly increases by r due to an increasing number of comparing graphs. To mitigate this problem, we utilize multiple particles' solutions instead of selecting only the best solution. While PSO's non-best solutions can be local optima, these solutions might contain interesting patterns that are similar to the best solutions to be found after many optimization repeats. Thus, after the final iteration, FEALM-UMAP stores s randomly-sampled non-best particles' solutions (e.g., 20 of 500 particles). Then, after r repeats, including the best solution, we have $r(1 + s)$ projections. From these, FEALM-UMAP recommends a user-specified small number of projections (e.g., 30 projections). For this recommendation, by default, we compare a set of DR results, \mathcal{Y} , instead of a set of graphs, \mathcal{G} . This is because

now we apply f_{DR} only to $r(1+s)$ projected datasets once (i.e., not involving the iterative optimization). For the comparison of \mathcal{Y} , we also use NSD on k -NN graphs constructed based on DR results (i.e., $d_{DR}(\mathbf{Y}_i, \mathbf{Y}_j) = d_{NSD}(f_{Gr}(\mathbf{Y}_i), f_{Gr}(\mathbf{Y}_j))$). Then, we perform spectral clustering [63] to recommend a small number of projections that produce significantly different DR results. We further provide interactive visualizations to flexibly review more solutions, as described in Sect. 7.

5.4 Implementation Details and Complexity Analysis

Implementation. FEALM and FEALM-UMAP are implemented with Python and libraries for matrix computations and optimizations: NumPy/SciPy [81], Scikit-learn [66], and Pymanopt [76]. While many graph dissimilarities, including NetLSD, are available in *netrd* [58], we use our implementation, which fully utilizes matrix computations to achieve faster calculation (e.g., our implementation of NetLSD is approximately 20 times faster than the one in *netrd* [1]). This is important as FEALM-UMAP involves a massive amount of graph comparisons (e.g., 10,000 times when using 500 particles and 20 iterations). Moreover, Pathos [60] is utilized to use multiprocessing for PSO.

Complexity analysis. We first discuss time complexity. The k -NN graph construction is used for f_{Gr} , which has $\mathcal{O}(n \log(n)m)$ with a ball-tree method [66]. NSD is composed of NetLSD ($\mathcal{O}(n^3)$) and ND ($\mathcal{O}(n^2k)$); therefore, it has $\mathcal{O}(n^3)$. Thus, when computing the best solution with PSO, the cost calculation by each particle at each iteration takes $\mathcal{O}(rn^3)$, where r is the number of produced graphs so far (i.e., NetLSD is the bottleneck). For space complexity, the main space use is by matrix multiplications in NetLSD and ND, which take $\mathcal{O}(n^2)$ space. During PSO, this amount of space is used by each particle. Based on the above analysis, we should use the maximum amount of available processes for PSO’s particles as long as there is enough memory space for matrix multiplications. For the utilization of non-best solutions, practically, UMAP becomes a computational bottleneck. UMAP is applied to $r(1+s)$ matrices with the size of $n \times m'$.

6 COMPUTATIONAL EVALUATIONS

We evaluate the performance of computations related to FEALM-UMAP as well as the design of ND by comparing it with SnC [43]. As an experimental platform, we used the MacBook Pro (16-inch, 2019) with 2.3 GHz 8-Core Intel Core i9 (16 threads) and 64 GB 2,667 MHz DDR4. We prepared datasets with the data generation code provided in Fujiwara et al. [27]. From the 20 Newsgroups dataset [21], their code can generate data with various numbers of instances (documents) and attributes (topics) by utilizing the latent Dirichlet allocation [10]. All source code used for the evaluations is available online [1].

Performance of f_{DR} , f_{Gr} , and d_{Gr} . We first evaluate the efficiency of each function related to Eq. 1 and 2, specifically, UMAP (f_{DR}), k -NN graph construction (f_{Gr}), ND (d_{ND}), NetLSD (d_{SD}), NSD (d_{NSD}), and SnC. As discussed, the number of instances, n , dominates these functions’ complexities. Thus, we ran the functions with different n ($n = 100, \dots, 1600$) but fixed k and m : $k = 15$ (UMAP’s default) and $m = 10$. Also, as we expect many executions by PSO’s particles, we measured the completion time of 100 executions. For the graph dissimilarity measures, we used our implementation described in Sect. 5.4.

First, as expected, UMAP and SnC spent much longer completion time than others: e.g., 152 and 52 seconds, respectively, for 100 executions when $n = 50$. Therefore, these functions are not suitable to use optimizations that require many executions or deal with a larger n —this is the reason why we have designed Eq. 2 and ND. Other functions’ completion times are shown in Fig. 5-a. We observe that, as n increases, d_{SD} (NetLSD) requires more computations, and dominates the completion time of d_{NSD} . However, 100 executions of d_{NSD} still can be completed within 20 seconds when $n = 1,600$.

Comparison of ND and SnC. We have introduced ND as a faster, more stable alternative to SnC. Here we validate that ND and SnC similarly capture the neighbor changes. Analogous to ND’s $\|\mathbf{D}_{i,j}^+\|_F$ and $\|\mathbf{D}_{i,j}^-\|_F$, SnC produces two distinct values, the steadiness and cohesiveness. We define the SnC-based dissimilarity measure as $d_{SnC} = 1 - \min(\text{steadiness}, \text{cohesiveness})$. Note that steadiness and

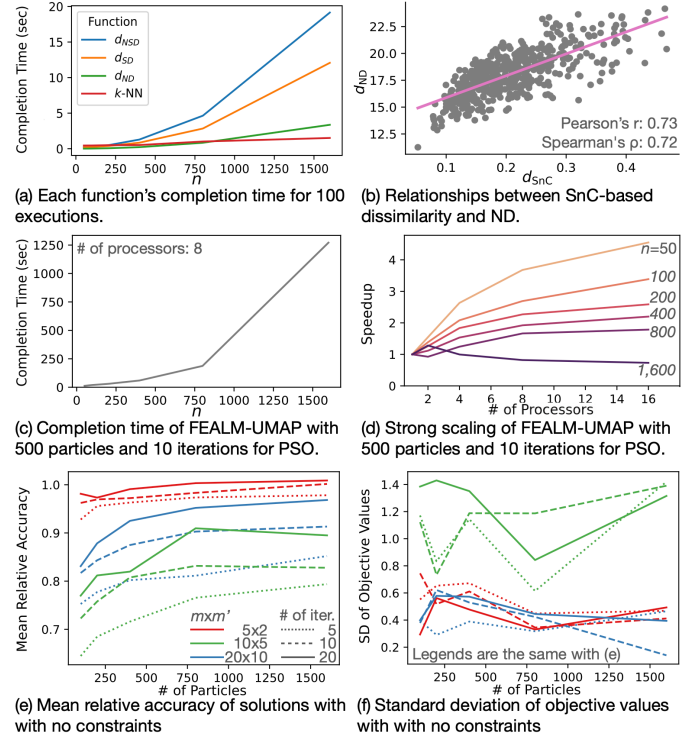


Fig. 5: Computational evaluation results.

cohesiveness take a range of 0–1; the larger, the fewer changes. For this experiment, we set $n = 200, m = 10$, and $k = 15$ and randomly generated 500 different projection matrices with the size of 10×5 and graphs corresponding to the projection matrices (with $f_{Gr}(\mathbf{X}^P)$).

Fig. 5-b shows d_{ND} and d_{SnC} of a graph corresponding to the original data and each of the 500 generated graphs. As SnC contains the randomness and d_{SnC} can be inconsistent, we took the mean of 50 executions in Fig. 5-b. The mean d_{SnC} of 50×500 results was 0.20 and the mean of 500 standard deviations was 0.02 (i.e., 10% of the mean). Fig. 5-b presents strong correlations between d_{ND} and d_{SnC} with Pearson’s and Spearman’s correlation coefficients of 0.73 and 0.72, respectively. This concludes that, similar to SnC, ND captures the neighbor changes, while ND has no randomness and a significantly smaller computational cost (as discussed, SnC takes 52 seconds for 100 executions when $n = 50$, for which ND takes 0.02 seconds). ND’s strengths enable us to provide computationally efficient, stable NSD.

Performance and scalability of the optimization. We evaluate the performance of FEALM-UMAP as a whole. For this experiment, we did not apply the utilization of non-best solutions as its computation is mainly dominated by UMAP. Similar to the experiments above, we tested multiple n with $k = 15, m = 10, m' = 5$, and no constraint on a projection matrix. Also, for PSO, we set 500 and 10 as the numbers of particles and iterations, respectively. We generated a single UMAP result that is different from the one using the original data (i.e., $r = 1$). We also used a different number of processors (from 1 to 16) to review FEALM-UMAP’s strong scaling (i.e., the completion time changes with the number of processors).

The result using 8 processors is shown Fig. 5-c. We can see when n is relatively small, FEALM-UMAP can produce a DR result in an acceptable completion time (e.g., 190 seconds when $n = 800$). Fig. 5-d shows speedups relative to when using a single processor. When the problem size and the number of used processors are relatively small, we can see reasonable scalability (e.g., when $n = 100$, the speedup is 2.7 with 8 processors). However, as the problem size increases, the speedup becomes more modest. When $n = 1,600$, we can see the performance decrease. We consider that this was caused by the large numbers of particles and processors, both of which occupied large memory space.

Quality of the optimization. Similar to the above experiment, we generated a single UMAP result with no constraint. For this experi-

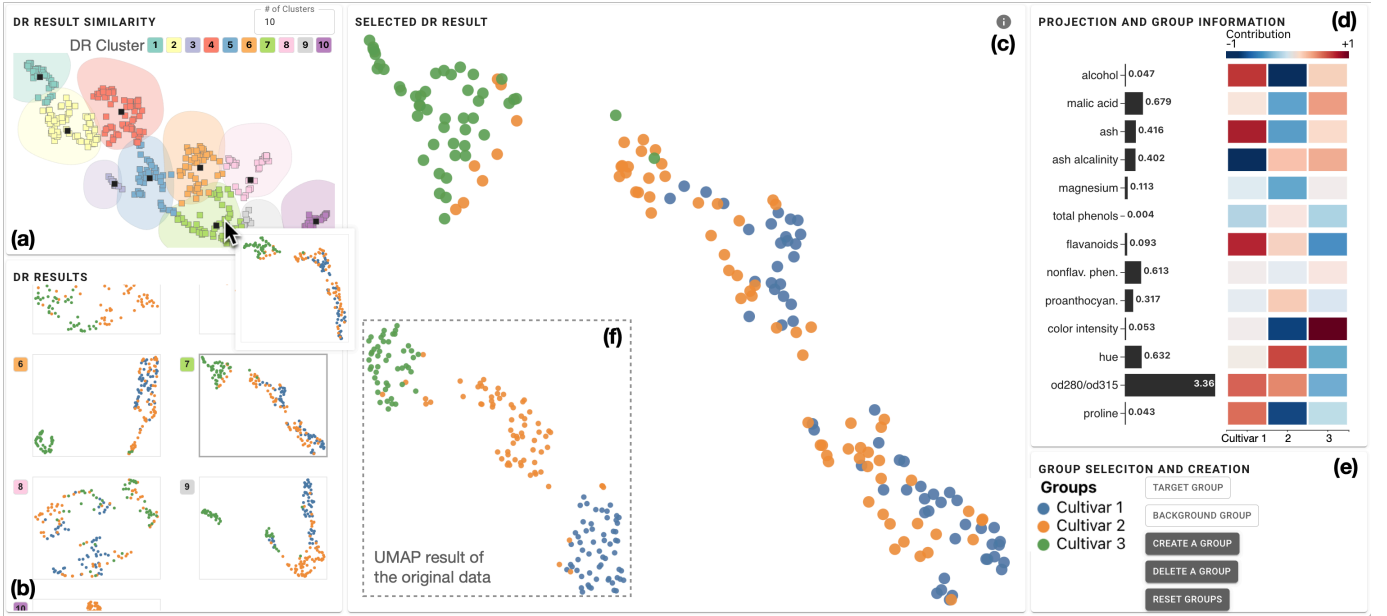


Fig. 6: Analyzing the Wine dataset [21] with FEALM-UMAP and the UI. The UI shows the similarities of the generated DR results (a), a representative subset of the DR results (b), a single selected DR result (c), the information for interpreting the DR result (d), and the group information (e). The DR result of the original data is also shown as a reference (f).

ment, we used the same number of instances ($n=400$) but a different number of attributes ($m=5, 10, 20$). We set m' approximately 50% of m ($m'=2, 5, 10$). Also, to see the effect of PSO's hyperparameters on the optimization quality, we tested different numbers of particles (from 100 to 1,600) and iterations (5, 10, and 20). As we do not know the truly best solution, we analyzed relative accuracy to the optimized solution with large numbers of particles and iterations, specifically, 3,200 particles and 40 iterations. Let v and v_{opt} be objective values of Eq. 2 for a comparing solution and the solution optimized with 3200 particles and 40 iterations, respectively; then, the relative accuracy is v/v_{opt} . As PSO's solutions can be varied based on the initialization, we computed the mean of relative accuracies for 10 trials.

Fig. 5-e shows the mean relative accuracy. Generally, the increase in the numbers of particles and iterations seems to improve the solutions. Also, we observe that the relative accuracy tends to be higher for the 20×10 searching space (blue lines) than the 10×5 searching space (green lines). For the 10×5 searching space, the accuracy relative to v_{opt} is still low even when using 1,600 particles and 20 iterations. Thus, we should use even larger numbers of particles and iterations to obtain better solutions. On the other hand, for the 20×10 searching space, the relative accuracy reaches 0.97 with 1,600 particles and 20 iterations. We expect that this is caused by a small number of instances ($n = 400$) relative to the searching space. In such a case, various solutions can easily produce a graph that has a large dissimilarity from the graph corresponding to the original data. Based on the above observations, we consider that the analysis of the relative accuracy helps us decide a searching space (e.g., the selection of m' and constraints) based on a given dataset. For example, for the above case, we should avoid using the 20×10 searching space. Note that a similar analysis on the absolute accuracy is commonly performed for classification tasks [24, 37]. Lastly, as shown in Fig. 5-f, we review the stability of objective values obtained with PSO. In a range from 200 to 800 particles, we can see a decreasing trend in the standard deviation of the objective values. However, for the 10×5 searching space, when the number of iterations is either 5 or 10, this trend cannot be seen. This can be related to the fact that when the number of iterations is significantly small in comparison with the size of the searching space or the number of particles, PSO behaves similar to random search [70]. This also can explain the increase of the standard deviation in the 10×5 searching space when using 1,600 particles—rather than the iterative updates, the generation of many random initial solutions dominates the optimization quality. Analyses similar to the above can be effective to decide the numbers of particles

and iterations for a given problem.

7 VISUAL INTERFACE

To efficiently investigate the results generated by FEALM-UMAP, as shown in Fig. 6, we develop a visual user interface (UI), which is also applicable to other methods developed within FEALM. The UI is developed as a web application, using Python, JavaScript, and D3 [11]. We provide a supplementary demonstration video of the UI [1].

Exploration of DR results. The views in Fig. 6-a and b are designed for exploration and comparison of the DR results. Fig. 6-a visualizes the information obtained through the optimization described in Sect. 5.3, including the set of UMAP results (i.e., \mathcal{Y}), dissimilarities of each result (i.e., $d_{DR}(\mathbf{Y}_i, \mathbf{Y}_j)$), and spectral-clustering-based recommendations. To visually convey the dissimilarities of UMAP results, we generate a 2D plot by applying UMAP based on $d_{DR}(\mathbf{Y}_i, \mathbf{Y}_j)$ (i.e., UMAP on the UMAP results). In this plot, each *square* point corresponds to a single UMAP result and their spatial proximities represent the similarities of the corresponding UMAP results. We indicate each point's belonging cluster by coloring each point and the isocontour generated by Bubble Sets [16]. We use black color to distinguish the selected points, which initially correspond to the recommended UMAP results. We also support fundamental interactions, such as zooming and tooltipping for previewing UMAP results (e.g., one in Fig. 6-a). A scrollable view in Fig. 6-b shows the UMAP results corresponding to the original data (i.e., \mathbf{Y}_0) and the selected black points. Their belonging clusters are indicated with colored texts (e.g., 7 colored green). A *circle* point in each UMAP result represents a data instance. Also, we color these points based on their group labels with a different color scheme from Fig. 6-a. For the comparison, each instance's color is consistent across all the UMAP results. Analysts can select one UMAP result from this view for more detailed-level investigations, as explained below.

Interpretation of a DR result. To help interpret the selected UMAP result, the view in Fig. 6-d shows the auxiliary information on (1) the projection matrix used to generate the UMAP result and (2) each attribute's contribution to the characteristics of groups in the UMAP result.

The projection matrix contains the information of more (dis)regarded attributes for the generation of the result. This information is useful to understand the cause of the selected UMAP result's difference from the others. As described in Sect. 4.2, a learnt projection matrix, \mathbf{P} , can be either diagonal (i.e., $\mathbf{P} = \text{diag}(\mathbf{w})$) or dense (i.e., when using no constraint or the constraint of $\mathbf{P} = \text{diag}(\mathbf{w})\mathbf{M}\text{diag}(\mathbf{v})$). When $\mathbf{P} = \text{diag}(\mathbf{w})$, we visualize values of \mathbf{w} as a bar chart, as shown on the left

side of Fig. 6-d. For the other case, we visualize values in \mathbf{P} as a heatmap using a gray scale (e.g., Fig. 8-e2 (left)).

Reviewing patterns shown in the DR result is essential to uncover analytical insights as well as to avoid deriving insights from false patterns due to excessive data transformation. The patterns are often examined through the comparison of data groups in the DR result [14, 25, 64]. To assist group comparison, as shown on the right side of Fig. 6-d, the UI integrates an existing contrastive-learning-based interpretation method, called ccPCA, and the heatmap-based visualization [25]. ccPCA contrasts a target group with a background group to reveal highly-contributed attributes to the characteristics of the target. The attributes' contributions are obtained as a weight vector, where the larger magnitude, the stronger contribution to the target group's characteristics. In addition, the sign of the weight vector can represent the direction of the contribution when using the sign adjustment method [26]. For example, while `alcohol` in Fig. 6-d contributes to the characteristics of both Cultivar 1 and 2, according to their sign, they likely have higher and lower alcohol percentages than others, respectively. Also, to enable the comparison of attribute values of instances, we update the size of each point in Fig. 6-c, when a certain attribute name is hovered in Fig. 6-d.

Although the UI uses predefined labels by default (e.g., the cultivar classes in Fig. 6), interactive refinement of groups can be performed with the lasso-selection available in Fig. 6-c and controls shown in Fig. 6-e. The changes in groups automatically update the attributes' contributions in Fig. 6-d. By default, when computing the contributions with ccPCA, each group is selected as a target group and the other groups are set as one background group. However, the UI also allows the analyst to explicitly select a background group. This functionality is useful when the comparison of two specific groups is more desired.

Through a collective use of the above functionalities and visualizations, we can thoroughly assess the DR result and patterns. When the observed groups do not result from false patterns, the projection matrix values, attributes' contributions, and distribution of attribute values should show some consistency. This is because the separation visible in the DR result should be highly related to the projection matrix, the differences should be captured in the attributes' contributions, and the attributes' contributions should reflect the attribute value distribution. We provide a concrete example by referring to Fig. 7 in the next section.

8 CASE STUDIES

As it is difficult to computationally evaluate an analytical value of DR results produced by FEALM-UMAP, we demonstrate the effectiveness of our approach through case studies on real-world datasets. Throughout all case studies, we generate UMAP results using two different constraints: $\mathbf{P} = \text{diag}(\mathbf{w})$ and $\mathbf{P} = \text{diag}(\mathbf{w})\mathbf{M}\text{diag}(\mathbf{v})$. Here we only describe the essential information to present the analysis results. We provide all the other details and one additional case study in the supplementary materials [1]. Note that the patterns uncovered in the case studies are difficult to identify with the aforesaid optimization method by Lehmann and Theisel [53] or attribute selection (refer to [1]).

8.1 Case Study 1: Diverse Categorization of Wines

We analyze the Wine dataset [21], which consists of 178 instances, 13 attributes, and cultivar labels. As shown in Fig. 6-f, DR on this dataset usually reveals three clusters highly related to the cultivars. With FEALM-UMAP, we seek patterns different from the typical clusters.

As shown in Fig. 6-b, FEALM-UMAP produces the results with greatly different patterns. We select a UMAP result with three clusters (Fig. 6-c), each of which is composed of multiple cultivars. As shown in Fig. 7-a1, we interactively define these clusters as Groups A–C. From the auxiliary information displayed in Fig. 7-a2, the UMAP result is generated with the constraint of $\mathbf{P} = \text{diag}(\mathbf{w})$, where `malic acid`, `hue`, and `nonflav. phen.` have considerable weights, while `od280/od315` has a dominant weight. Also, `od280/od315` shows a strong contribution to each clusters' characteristics (see Fig. 7-a2(right)). As shown in Fig. 7-a1, we further verify the strong associations between the clusters and `od280/od315`'s value distribution (e.g., Group A has small

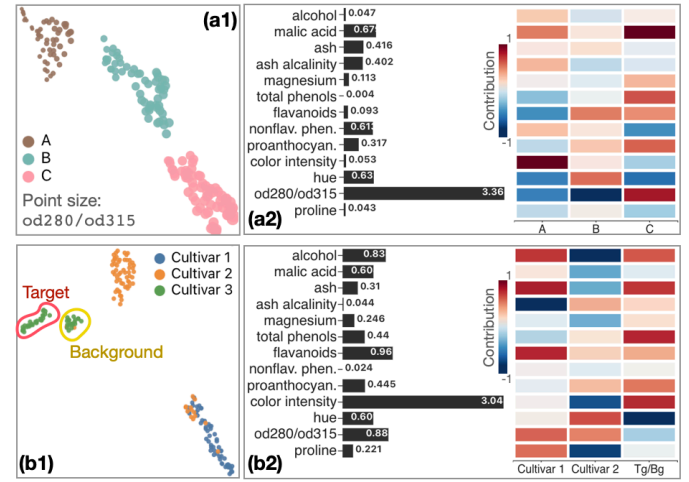


Fig. 7: Study 1: Diverse categorizations of wines. DR results selected from the Fig. 6-b (a1, b1) and their auxiliary information (a2, b2).

`od280/od315` values). While `od280/od315` is to measure the appearance of wine (specifically, cloudiness), it is also known to show a strong correlation to taste-related measures (e.g., `total phenols`) [7]. By emphasizing `od280/od315` while still utilizing other attributes, FEALM-UMAP seems to find a new categorization of wines. As observed from the attributes' contributions, the new categorization is related less to alcohol/fermentation (i.e., `alcohol` and `proline`) and mineral content attributes (i.e., `ash`, `ash alkalinity`, and `magnesium`) but more to appearance and taste (i.e. the rest of the attributes).

We also find that the DR result in Fig. 7-b1 separates Cultivar 3 (green) from others more clearly than the one in Fig. 6-f. Thus, data scaling shown in Fig. 7-b2 can be useful when performing the classification of Cultivar 3 wines and the others (i.e., not the classification of all the cultivars). Since we can also see two subclusters of Cultivar 3, we select them as target and background groups (Tg and Bg) to further investigate their difference. From Tg/Bg column in Fig. 7-b2, these can be expected to have the differences in colors (`color intensity` and `hue`) and some other profiles (e.g., `total phenols`). FEALM-UMAP seems to find subcategorization of Cultivar 3, which was obscured when focusing on all the attributes equally.

8.2 Case Study 2: Identification of Hidden Political Groups

We analyze the PPIC Statewide Survey October 2018 [6], which contains California residents' political opinions. We specifically analyze the version prepared with the standard preprocessing (e.g., handling missing values) [27]. This version contains 548 instances/residents and 27 attributes/questions. As in the work by Hare et al. [32], DR on data of American voters often only reveals two clusters highly related to the left-right ideology. In fact, as shown in Fig. 8-a, when applying UMAP to the dataset as is, we can only see such clusters highly corresponded to the Democrat (Dem) and Republican (Rep) supporters. We utilize FEALM-UMAP to reveal political groups hidden in the data.

Fig. 8-b shows the similarities of the generated UMAP results. We first notice the clear separation between DR Clusters 1–2 and the others. By interactively previewing the UMAP results, we observe that the results in DR Clusters 1 and 2 always show many small instance clusters (e.g., Fig. 8-c(left)). These patterns are likely related to the case FEALM-UMAP only emphasizes questions on which the residents have varied opinions. Also, through the interactive exploration, we notice that many UMAP results still show the clusters of Dem and Rep (e.g., Fig. 8-c(right)). This implies the difficulty of finding different grouping patterns from this dataset. However, we still see different patterns in some of the DR results. For example, Fig. 8-c(center) shows four clusters, Groups A–D. While Group A and Group B mainly include Rep and Dem, respectively, Groups C and D contain both Rep and Dem.

To investigate this UMAP result, we interactively create the corresponding groups (Fig. 8-d1) and obtain the auxiliary information. From Fig. 8-d2, both the weight vector (shown as a bar chart) and attributes' contributions (shown as a blue-red heatmap) indicate that the forma-

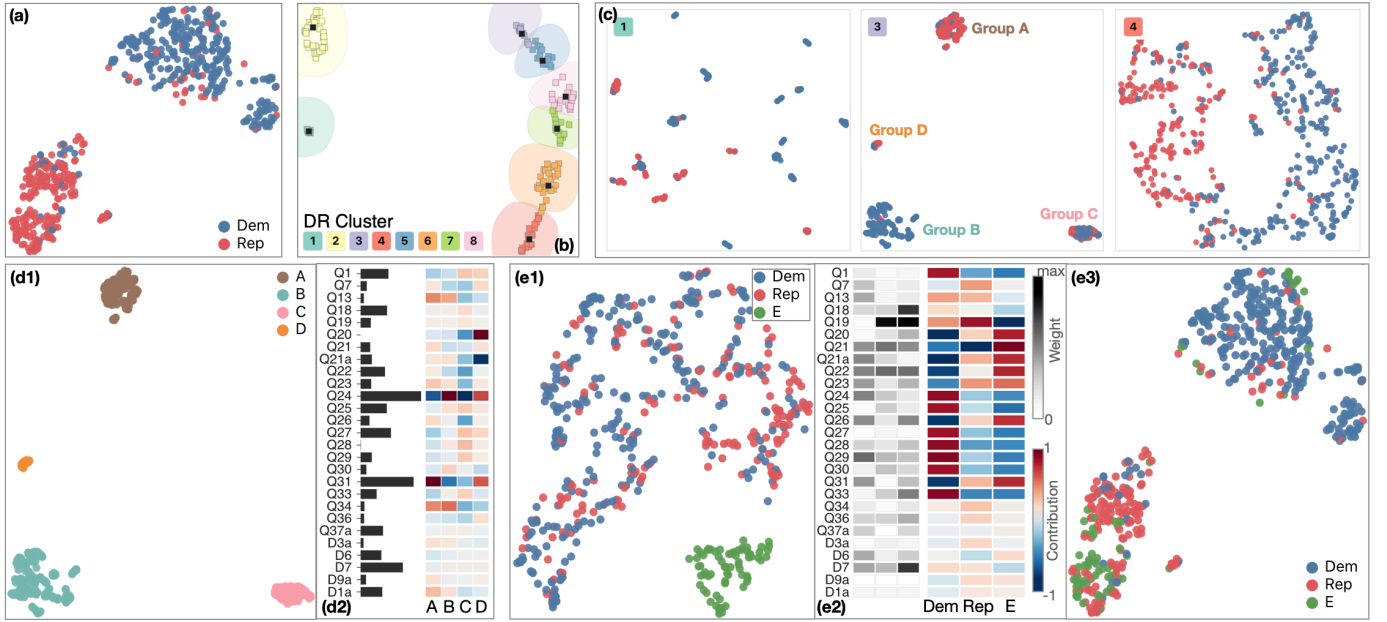


Fig. 8: Study 2: Identification of hidden political subgroups. The original UMAP result (a), similarities of the generated UMAP results (b), three representative DR results (c), redefined groups from one of the DR results (d1), the auxiliary information of d1 (d2), another result selected through the exploration of the DR results (e1, e2), and the original UMAP result using the same grouping with e1 (e3).

tion of Groups A–D is highly related to Q24 and Q31; these questions are on the preference of the government size (smaller or bigger) and the impression of the Republican party (favorable or unfavorable), respectively. The four clusters are likely formed because of the binary questions. Although the cause of the four clusters is simple, we can still gain useful information. By interactively reviewing the two attributes’ values, we observe that a relatively large cluster, Group C, has a preference for a smaller government and an unfavorable impression of the Republican party. Thus, in California in 2018, a considerable portion of the Republican supporters seems to have an unfavorable impression of their supporting party. A similar conclusion can be made for the Democrat supporters’ opinions on the government size.

To find further interesting patterns, we interactively preview various UMAP results, using the view in Fig. 8-b. From DR Cluster 4, we see a DR result with two clear clusters, as shown in Fig. 8-e1. Within this DR result, we create Group E by selecting a smaller cluster, where the majority of instances were from Rep. As the auxiliary information shows the gray heatmap (Fig. 8-e2), this DR result is generated with the projection where $\mathbf{P} = \text{diag}(\mathbf{w})\mathbf{M}\text{diag}(\mathbf{v})$. While some questions, such as Q19 (the housing affordability), have large weights, we can see many questions are utilized for this UMAP result (e.g., the rows from Q18 to Q33). The attributes’ contributions highlight obvious differences between Dem and Group E: Almost all the contributions have opposite signs but show similar magnitudes. Therefore, we can expect that Group E consists of the residents whose political opinions are largely different from the majority of the Democrat supporters. As shown in Fig. 8-e3, this political group was not clearly captured by the original UMAP, while some localization of Group E can be seen.

9 DISCUSSION

FEALM and FEALM-UMAP have provided a primary step in addressing the aforesaid problem of hidden manifolds. We discuss our approach’s current limitations as observed through the theoretical and experimental analyses, and discuss further potential enhancements.

Scalability. As discussed in Sect. 5.4 and Sect. 6, FEALM-UMAP has limited scalability for the numbers of instances (n) and attributes (m). Because of NSD’s time and space complexities ($\mathcal{O}(n^3)$ and $\mathcal{O}(n^2)$, respectively), FEALM-UMAP is computationally expensive when n is large. Based on the results in Sect. 6, FEALM-UMAP is practical up until data with a few thousand instances when using a mid-range computer. When m is large, on the other hand, the search space becomes very large; consequently, PSO requires large numbers of particles and

iterations to find solutions of adequate quality. As PSO’s algorithm is inherently parallel—each particle finds one solution, parallel computing could provide better scalability. However, as shown, the space occupation by particles is the obstacle to this approach. We plan to develop a more space-efficient optimization (e.g., by actively discarding particles during the optimization) as well as perform experiments using multiprocessor systems and large memory areas, such as supercomputers and distributed high throughput systems [71]. Another potential approach is to make all functions differentiable and use derivative-based solvers. We expect that this can be achieved by utilizing differentiable variants of k -neighbor selections [67] as well as developing NSD for weighted graphs. While the equations used in ND and NetLSD [77] can be naturally extended weighted graphs, we need further investigations to understand their characteristics in the context of weighted graphs.

Robustness and reliability. The scalability issues also influence the robustness and reliability of FEALM-UMAP. The quality of solutions can vary based on the random initialization of PSO’s particles. To obtain more consistent, reasonable solutions, many particles for large m should be used; however, this easily leads to a vast amount of particles. For example, when we produce a projection matrix with a size of 30×10 (i.e., $m = 30$ and $m' = 10$), assigning 100 particles per parameter involves 30,000 particles, which requires substantial memory space. Thus, to perform robust analyses when m is large (e.g., $m > 30$), we require either limiting the projection matrix size (by allowing only data scaling or using small m') or repeating the PSO many times with a small number of particles. As for the reliability of the generated DR results, similar to other ML methods, FEALM-UMAP could suffer from overfitting when n is relatively small compared to m [31] (as seen in Sect. 6). Therefore, FEALM-UMAP is suitable for data where n is considerably larger than m (e.g., $n = 1000$, $m = 20$). When n is relatively small, we can define stronger constraints on the projection matrix (e.g., only data scaling) and/or primarily apply other linear DR (e.g., PCA) to reduce m . To further reduce the risk of false findings, our visual interface also assists the user to inspect the obtained DR results.

Generalizability. FEALM is designed as a general framework for nonlinear DR methods. We emphasize that FEALM is applicable to various nonlinear DR methods, such as t-SNE, as discussed in Sect. 5. FEALM can also be used for linear DR methods. For example, Eq. 1 can be applied to the linear DR method designed by Lehmann and Theisel [53]. Furthermore, we can extend Eq. 2 to recommend sets of graph-related hyperparameters of DR (e.g., the number of neighbors in UMAP), which produce significantly different DR results [15]. This can be

achieved by replacing a linear projection matrix with hyperparameters for search parameters.

10 CONCLUSION

We have presented FEALM, a feature learning framework that enables investigation of data patterns via a conjoint use with nonlinear DR. The derived exemplifying method and visual interface have demonstrated the effectiveness of FEALM for analyses of real-world datasets. This work also exposes the limitations of conventional ways of data exploration using dimensionality reduction and thus contributes toward maximal utilization of data.

ACKNOWLEDGMENTS

This work has been supported by the Knut and Alice Wallenberg Foundation through Grant KAW 2019.0024, the U.S. National Science Foundation through Grant IIS-1741536, and a gift grant provided by Bosch Research.

REFERENCES

- [1] The supplementary materials: The demonstration video of the visual interface, source code, evaluation details, and supplemental evaluation. <https://takanori-fujiwara.github.io/s/fealm/>.
- [2] A. Abid, M. J. Zhang, V. K. Bagaria, and J. Zou. Exploring patterns enriched in a dataset with contrastive principal component analysis. *Nat. Commun.*, 9(1):2134, 2018.
- [3] P.-A. Absil, R. Mahony, and R. Sepulchre. *Optimization algorithms on matrix manifolds*. Princeton University Press, 2009.
- [4] P.-A. Absil, R. Mahony, and J. Trumpf. An extrinsic look at the Riemannian Hessian. In *Proc. GSI*, pp. 361–368. Springer, 2013.
- [5] D. Asimov. The Grand Tour: A tool for viewing multidimensional data. *SIAM J. Sci. Comput.*, 6(1):128–143, 1985.
- [6] M. Baldassare, D. Bonner, A. Dykman, and L. Lopes. PPIC statewide survey: Californians & their government, October 2018. Report: <https://www.ppic.org/wp-content/uploads/ppic-statewide-survey-october-2018.pdf>, Dataset: <https://www.ppic.org/data-set/ppic-statewide-survey-data-2018/>, 2018. Accessed: 2021-3-21.
- [7] J. Barth, D. Katumullage, C. Yang, and J. Cao. Classification of wines using principal component analysis. *J. Wine Econ.*, 16(1):56–67, 2021.
- [8] C. Baumgartner, C. Plant, K. Railing, H.-P. Kriegel, and P. Kroger. Subspace selection for clustering high-dimensional data. In *Proc. ICDM*, pp. 11–18, 2004.
- [9] E. Becht, L. McInnes, J. Healy, C.-A. Dutertre, I. W. Kwok, L. G. Ng, F. Ginhoux, and E. W. Newell. Dimensionality reduction for visualizing single-cell data using UMAP. *Nat. Biotechnol.*, 37(1):38–44, 2019.
- [10] D. M. Blei, A. Y. Ng, and M. I. Jordan. Latent Dirichlet allocation. *J. Mach. Learn. Res.*, 3:993–1022, 2003.
- [11] M. Bostock, V. Ogievetsky, and J. Heer. D³ data-driven documents. *IEEE Trans. Vis. Comput. Graph.*, 17(12):2301–2309, 2011.
- [12] N. Boumal, B. Mishra, P.-A. Absil, and R. Sepulchre. Manopt, a Matlab toolbox for optimization on manifolds. *J. Mach. Learn. Res.*, 15(1):1455–1459, 2014.
- [13] J. Bradbury, R. Frostig, P. Hawkins, M. J. Johnson, C. Leary, D. Maclaurin, G. Necula, A. Paszke, J. VanderPlas, S. Wanderman-Milne, and Q. Zhang. JAX: Composable transformations of Python+NumPy programs, 2018.
- [14] M. Brehmer, M. Sedlmair, S. Ingram, and T. Munzner. Visualizing dimensionally-reduced data: Interviews with analysts and a characterization of task sequences. In *Proc. BELIV*, pp. 1–8, 2014.
- [15] A. Chatzimpampas, R. M. Martins, and A. Kerren. t-viSNE: Interactive assessment and interpretation of t-sne projections. *IEEE Trans. Vis. Comput. Graph.*, 26(8):2696–2714, 2020.
- [16] C. Collins, G. Penn, and S. Carpendale. Bubble Sets: Revealing set relations with isocontours over existing visualizations. *IEEE Trans. Vis. Comput. Graph.*, 15(6):1009–1016, 2009.
- [17] J. P. Cunningham and Z. Ghahramani. Linear dimensionality reduction: Survey, insights, and generalizations. *J. Mach. Learn. Res.*, 16(1):2859–2900, 2015.
- [18] A. Dasgupta and R. Kosara. Pargnostics: Screen-space metrics for parallel coordinates. *IEEE Trans. Vis. Comput. Graph.*, 16(6):1017–1026, 2010.
- [19] D. L. Donoho et al. High-dimensional data analysis: The curses and blessings of dimensionality. *AMS Math Challenges Lecture*, 1(2000):32, 2000.
- [20] M. W. Dorrity, L. M. Saunders, C. Queitsch, S. Fields, and C. Trapnell. Dimensionality reduction by UMAP to visualize physical and genetic interactions. *Nat. Commun.*, 11(1):1–6, 2020.
- [21] D. Dua and C. Graff. UCI machine learning repository. <http://archive.ics.uci.edu/ml>, 2019.
- [22] L. Ertöz, M. Steinbach, and V. Kumar. Finding clusters of different sizes, shapes, and densities in noisy, high dimensional data. In *Proc. SDM*, pp. 47–58. SIAM, 2003.
- [23] M. Espadoto, R. M. Martins, A. Kerren, N. S. T. Hirata, and A. C. Telea. Toward a quantitative survey of dimension reduction techniques. *IEEE Trans. Vis. Comput. Graph.*, 27(3):2153–2173, 2021.
- [24] R. L. Figueroa, Q. Zeng-Treitler, S. Kandula, and L. H. Ngo. Predicting sample size required for classification performance. *BMC Medical Inform. Decis. Mak.*, 12(1):1–10, 2012.
- [25] T. Fujiwara, O.-H. Kwon, and K.-L. Ma. Supporting analysis of dimensionality reduction results with contrastive learning. *IEEE Trans. Vis. Comput. Graph.*, 26(1):45–55, 2020.
- [26] T. Fujiwara, Shilpika, N. Sakamoto, J. Nonaka, K. Yamamoto, and K.-L. Ma. A visual analytics framework for reviewing multivariate time-series data with dimensionality reduction. *IEEE Trans. Vis. Comput. Graph.*, 27(2):1601–1611, 2021.
- [27] T. Fujiwara, X. Wei, J. Zhao, and K.-L. Ma. Interactive dimensionality reduction for comparative analysis. *IEEE Trans. Vis. Comput. Graph.*, 28(1):758–768, 2022.
- [28] S. García, J. Luengo, and F. Herrera. *Data preprocessing in data mining*, vol. 72. Springer, 2015.
- [29] M. Gleicher. Explainers: Expert explorations with crafted projections. *IEEE Trans. Vis. Comput. Graph.*, 19(12):2042–2051, 2013.
- [30] C. Goodall. Procrustes methods in the statistical analysis of shape. *J. R. Stat. Soc. Series B: Stat. Methodol.*, 53(2):285–321, 1991.
- [31] Y. Guo, T. Hastie, and R. Tibshirani. Regularized linear discriminant analysis and its application in microarrays. *Biostatistics*, 8(1):86–100, 2007.
- [32] C. Hare, T.-P. Liu, and R. N. Lupton. What Ordered Optimal Classification reveals about ideological structure, cleavages, and polarization in the American mass public. *Public Choice*, 176(1):57–78, 2018.
- [33] J. A. Hartigan. Printer graphics for clustering. *J. Stat. Comput. Simul.*, 4(3):187–213, 1975.
- [34] T. Hastie and R. Tibshirani. Discriminant analysis by Gaussian mixtures. *J. R. Stat. Soc. B*, pp. 155–176, 1996.
- [35] F. Hohman, H. Park, C. Robinson, and D. H. P. Chau. Summit: Scaling deep learning interpretability by visualizing activation and attribution summarizations. *IEEE Trans. Vis. Comput. Graph.*, 26(1):1096–1106, 2020.
- [36] H. Hotelling. Analysis of a complex of statistical variables into principal components. *J. Educ. Psychol.*, 24(6):417, 1933.
- [37] J. Hua, Z. Xiong, J. Lowey, E. Suh, and E. R. Dougherty. Optimal number of features as a function of sample size for various classification rules. *Bioinformatics*, 21(8):1509–1515, 2005.
- [38] P. J. Huber. Projection pursuit. *Ann. Stat.*, pp. 435–475, 1985.
- [39] M. Hund, D. Böhm, W. Sturm, M. Sedlmair, T. Schreck, T. Ullrich, D. A. Keim, L. Majnarić, and A. Holzinger. Visual analytics for concept exploration in subspaces of patient groups. *Brain Inform.*, 3(4):233–247, 2016.
- [40] A. Inselberg and B. Dimsdale. Parallel coordinates for visualizing multi-dimensional geometry. In *Proc. Computer Graphics*, pp. 25–44. Springer, 1987.
- [41] A. J. Izenman. Linear discriminant analysis. In *Modern Multivariate Statistical Techniques*, pp. 237–280. Springer, 2013.
- [42] D. Jäckle, M. Hund, M. Behrisch, D. A. Keim, and T. Schreck. Pattern Trails: Visual analysis of pattern transitions in subspaces. In *Proc. VAST*, pp. 1–12. IEEE, 2017.
- [43] H. Jeon, H.-K. Ko, J. Jo, Y. Kim, and J. Seo. Measuring and explaining the inter-cluster reliability of multidimensional projections. *IEEE Trans. Vis. Comput. Graph.*, 28(1):551–561, 2022.
- [44] D. H. Jeong, C. Ziemkiewicz, B. Fisher, W. Ribarsky, and R. Chang. iPCA: An interactive system for PCA-based visual analytics. *Comput. Graph. Forum*, 28(3):767–774, 2009.
- [45] I. T. Jolliffe. *Principal Component Analysis and Factor Analysis*, pp. 115–128. Springer, 1986.
- [46] I. T. Jolliffe and J. Cadima. Principal component analysis: A review and recent developments. *Philos. Trans. R. Soc. A: Math. Phys. Eng. Sci.*, 374(2065):20150202, 2016.

- [47] M. C. Jones and R. Sibson. What is projection pursuit? *J. R. Stat. Soc. A-G.*, 150(1):1–18, 1987.
- [48] J. Kennedy and R. Eberhart. Particle swarm optimization. In *Proc. ICNN*, vol. 4, pp. 1942–1948. IEEE, 1995.
- [49] D. Kobak and G. C. Linderman. Initialization is critical for preserving global data structure in both t-SNE and UMAP. *Nat. Biotechnol.*, 39(2):156–157, 2021.
- [50] J. Krause, A. Dasgupta, J.-D. Fekete, and E. Bertini. SeekAView: An intelligent dimensionality reduction strategy for navigating high-dimensional data spaces. In *Proc. LDAV*, pp. 11–19. IEEE, 2016.
- [51] H.-P. Kriegel, P. Kröger, and A. Zimek. Clustering high-dimensional data: A survey on subspace clustering, pattern-based clustering, and correlation clustering. *ACM Trans. Knowl. Discov. Data*, 3(1):1–58, 2009.
- [52] O.-H. Kwon, T. Crnovrsanin, and K.-L. Ma. What would a graph look like in this layout? A machine learning approach to large graph visualization. *IEEE Trans. Vis. Comput. Graph.*, 24(1):478–488, 2018.
- [53] D. J. Lehmann and H. Theisel. Optimal sets of projections of high-dimensional data. *IEEE Trans. Vis. Comput. Graph.*, 22(1):609–618, 2016.
- [54] S. Liu, P.-T. Bremer, J. Jayaraman, B. Wang, B. Summa, and V. Pascucci. The Grassmannian Atlas: A general framework for exploring linear projections of high-dimensional data. *Comput. Graph. Forum*, 35(3):1–10, 2016.
- [55] S. Liu, D. Maljovec, B. Wang, P.-T. Bremer, and V. Pascucci. Visualizing high-dimensional data: Advances in the past decade. *IEEE Trans. Vis. Comput. Graph.*, 23(3):1249–1268, 2016.
- [56] S. Liu, B. Wang, J. J. Thiagarajan, P.-T. Bremer, and V. Pascucci. Visual exploration of high-dimensional data through subspace analysis and dynamic projections. *Comput. Graph. Forum*, 34(3):271–280, 2015.
- [57] S. Marsland. *Machine learning: An algorithmic perspective*. Chapman and Hall/CRC, 2011.
- [58] S. McCabe, L. Torres, T. LaRock, S. A. Haque, C.-H. Yang, H. Hartle, and B. Klein. netrd: A library for network reconstruction and graph distances. *J. Open Source Softw.*, 6(62):2990, 2021.
- [59] L. McInnes, J. Healy, and J. Melville. UMAP: Uniform manifold approximation and projection for dimension reduction. *arXiv:1802.03426*, 2018.
- [60] M. M. McKerns, L. Strand, T. Sullivan, A. Fang, and M. A. Aivazis. Building a framework for predictive science. In *Proc. Python in Science Conference*, 2011.
- [61] S. Mika, G. Ratsch, J. Weston, B. Scholkopf, and K.-R. Mullers. Fisher discriminant analysis with kernels. In *Proc. IEEE Signal Processing Society Workshop*, pp. 41–48, 1999.
- [62] J. E. Nam and K. Mueller. Tripadvisor^{N-D}: A tourism-inspired high-dimensional space exploration framework with overview and detail. *IEEE Trans. Vis. Comput. Graph.*, 19(2):291–305, 2012.
- [63] A. Ng, M. Jordan, and Y. Weiss. On spectral clustering: Analysis and an algorithm. *Adv. Neural Inf. Process. Syst.*, 14, 2001.
- [64] L. G. Nonato and M. Aupetit. Multidimensional projection for visual analytics: Linking techniques with distortions, tasks, and layout enrichment. *IEEE Trans. Vis. Comput. Graph.*, 25(8):2650–2673, 2019.
- [65] L. Parsons, E. Haque, and H. Liu. Subspace clustering for high dimensional data: A review. *ACM SIGKDD Explorations Newsletter*, 6(1):90–105, 2004.
- [66] F. Pedregosa, G. Varoquaux, A. Gramfort, V. Michel, B. Thirion, O. Grisel, M. Blondel, P. Prettenhofer, R. Weiss, V. Dubourg, J. Vanderplas, A. Passos, D. Cournapeau, M. Brucher, M. Perrot, and E. Duchesnay. Scikit-learn: Machine learning in Python. *J. Mach. Learn. Res.*, 12:2825–2830, 2011.
- [67] T. Plötz and S. Roth. Neural nearest neighbors networks. *Adv. Neural Inf. Process. Syst.*, 31, 2018.
- [68] D. Sacha, L. Zhang, M. Sedlmair, J. A. Lee, J. Peltonen, D. Weiskopf, S. C. North, and D. A. Keim. Visual interaction with dimensionality reduction: A structured literature analysis. *IEEE Trans. Vis. Comput. Graph.*, 23(1):241–250, 2017.
- [69] N. Saeed, H. Nam, M. I. U. Haq, and D. B. Muhammad Saqib. A survey on multidimensional scaling. *ACM Comput. Surv.*, 51(3):1–25, 2018.
- [70] F. J. Solis and R. J.-B. Wets. Minimization by random search techniques. *Math. Oper. Res.*, 6(1):19–30, 1981.
- [71] E. Strohmaier, J. Dongarra, H. Simon, M. Meuer, and H. Meuer. The TOP500 supercomputer list. <http://www.top500.org>. Accessed: 2022-03-26.
- [72] G. Sun, S. Zhu, Q. Jiang, W. Xia, and R. Liang. EvoSets: Tracking the sensitivity of dimensionality reduction results across subspaces. *IEEE Trans. Big Data*, 2021 (early access).
- [73] M. Tantardini, F. Ieva, L. Tajoli, and C. Piccardi. Comparing methods for comparing networks. *Scientific Reports*, 9(1):1–19, 2019.
- [74] A. Tatu, F. Maaß, I. Färber, E. Bertini, T. Schreck, T. Seidl, and D. Keim. Subspace search and visualization to make sense of alternative clusterings in high-dimensional data. In *Proc. VAST*, pp. 63–72. IEEE, 2012.
- [75] W. S. Torgerson. Multidimensional scaling: I. theory and method. *Psychometrika*, 17(4):401–419, 1952.
- [76] J. Townsend, N. Koep, and S. Weichwald. Pymanopt: A python toolbox for optimization on manifolds using automatic differentiation. *J. Mach. Learn. Res.*, 17(137):1–5, 2016.
- [77] A. Tsitsulin, D. Mottin, P. Karras, A. Bronstein, and E. Müller. NetLSD: Hearing the shape of a graph. In *Proc. KDD*, pp. 2347–2356, 2018.
- [78] L. Van Der Maaten. Accelerating t-SNE using tree-based algorithms. *J. Mach. Learn. Res.*, 15(1):3221–3245, 2014.
- [79] L. van der Maaten and G. Hinton. Visualizing data using t-SNE. *J. Mach. Learn. Res.*, 9(Nov):2579–2605, 2008.
- [80] L. van der Maaten, E. Postma, and J. van den Herik. Dimensionality reduction: A comparative review. *Journal of Machine Learning Research*, 10:66–71, 2009.
- [81] P. Virtanen, R. Gommers, T. E. Oliphant, M. Haberland, T. Reddy, D. Cournapeau, E. Burovski, P. Peterson, W. Weckesser, J. Bright, et al. SciPy 1.0: Fundamental algorithms for scientific computing in Python. *Nat. Methods*, 17:261–272, 2020.
- [82] B. Wang and K. Mueller. The Subspace Voyager: Exploring high-dimensional data along a continuum of salient 3d subspaces. *IEEE Trans. Vis. Comput. Graph.*, 24(2):1204–1222, 2017.
- [83] Y. Wang, J. Li, F. Nie, H. Theisel, M. Gong, and D. J. Lehmann. Linear discriminative star coordinates for exploring class and cluster separation of high dimensional data. *Comput. Graph. Forum*, 36(3):401–410, 2017.
- [84] L. Wilkinson, A. Anand, and R. Grossman. High-dimensional visual analytics: Interactive exploration guided by pairwise views of point distributions. *IEEE Trans. Vis. Comput. Graph.*, 12(6):1363–1372, 2006.
- [85] S. Yan, D. Xu, B. Zhang, H.-J. Zhang, Q. Yang, and S. Lin. Graph embedding and extensions: A general framework for dimensionality reduction. *IEEE Trans. Pattern Anal. Mach. Intell.*, 29(1):40–51, 2006.
- [86] X. Yuan, D. Ren, Z. Wang, and C. Guo. Dimension Projection Matrix/Tree: Interactive subspace visual exploration and analysis of high dimensional data. *IEEE Trans. Vis. Comput. Graph.*, 19(12):2625–2633, 2013.
- [87] R. Zebari, A. Abdulazeez, D. Zeebaree, D. Zebari, and J. Saeed. A comprehensive review of dimensionality reduction techniques for feature selection and feature extraction. *J. Appl. Sci. Technol. Trends*, 1(2):56–70, 2020.
- [88] F. Zhou, J. Li, W. Huang, Y. Zhao, X. Yuan, X. Liang, and Y. Shi. Dimension reconstruction for visual exploration of subspace clusters in high-dimensional data. In *Proc. PacificVis*, pp. 128–135. IEEE, 2016.
- [89] J. Y. Zou, D. J. Hsu, D. C. Parkes, and R. P. Adams. Contrastive learning using spectral methods. In *Proc. NIPS*, pp. 2238–2246, 2013.